

## Flows in Enthalpy Based Thermal Evolution of Loops

ABHISHEK RAJHANS,<sup>1</sup> DURGESH TRIPATHI,<sup>1</sup> STEPHEN J. BRADSHAW,<sup>2</sup> VINAY L. KASHYAP,<sup>3</sup> AND JAMES A. KLIMCHUK<sup>4</sup>

<sup>1</sup>*Inter-University Centre for Astronomy and Astrophysics, Post Bag - 4, Ganeshkhind, Pune 411007, India*

<sup>2</sup>*Rice University, Department of Physics and Astronomy, 6100 Main Street Houston, TX 77004, USA*

<sup>3</sup>*Center for Astrophysics | Harvard & Smithsonian, 60 Garden St. Cambridge MA 02138, USA*

<sup>4</sup>*NASA Goddard Space Flight Center, Solar Physics Laboratory, Code 671, Greenbelt, MD 20771, USA*

(Received; Revised; Accepted)

Submitted to ApJ

### ABSTRACT

Plasma filled loop structures are common in the solar corona. Because detailed modeling of the dynamical evolution of these structures is computationally costly, an efficient method for computing approximate but quick physics-based solutions is to rely on space integrated 0D simulations. The enthalpy based thermal evolution of loops (EBTEL) framework is a commonly used method to study the exchange of mass and energy between the corona and transition region. EBTEL solves for density, temperature, and pressure, averaged over the coronal part of loop, velocity at coronal base, and the instantaneous differential emission measure distribution in the transition region. The current single-fluid version of the code, EBTEL2, assumes that at all stages the flows are subsonic. However, sometimes the solutions show the presence of supersonic flows during the impulsive phase of heat input. It is thus necessary to account for this effect. Here, we upgrade EBTEL2 to EBTEL3 by including the kinetic energy term in the Navier-Stokes equation. We compare the solutions from EBTEL3 with those obtained using EBTEL2 as well as the state-of-the-art field aligned hydrodynamics code HYDRAD. We find that the match in pressure between EBTEL3 and HYDRAD is better than that between EBTEL2 and HYDRAD. Additionally, the velocities predicted by EBTEL3 are in close agreement with those obtained with HYDRAD when the flows are subsonic. However, EBTEL3 solutions deviate substantially from HYDRAD's when the latter predicts supersonic flows. Using the mismatches in the solution, we propose a criterion to determine the conditions under which EBTEL can be used to study flows in the system.

### 1. INTRODUCTION

The Solar corona has a myriad of loop like structures, which are magnetic flux tubes filled with plasma. Field aligned hydrodynamic simulations serve as an efficient tool for studying the response of plasma in coronal loops to a generic time dependent heating event, (see eg., Klimchuk 2006, 2015; Reale 2014, for a review). However in situations where one needs to study the effects of variation of parameters like loop length, energy budget and profile of heating function, a large number of runs are required. Additionally more realistic scenarios involve multi-stranded loops as opposed to simple monolithic ones. Performing field aligned simulations for such complicated but realistic scenarios is computationally expensive. To overcome such issues, 0D codes have been developed. The idea is that in the coronal part, physical parameters do not vary much along the loop. Hence the values of average density, temperature and pressure are characteristic for the coronal part of the loop (see Cargill et al. 2012a, for a detailed discussion on various 0D models). In this work we restrict ourselves to the commonly used 0D code: Enthalpy Based Thermal Evolution of Loops (EBTEL; see Klimchuk et al. 2008; Cargill et al. 2012b; Barnes et al. 2016, for details).

In a nutshell, EBTEL studies the mass and energy exchange between the corona and the transition region. It calculates average temperature, density, pressure, and velocity at the base of the coronal loops. It also computes the instantaneous differential emission measure in the transition region. The coronal base of a loop is defined as the position at which

thermal conduction changes from cooling term to heating term. Mathematically, this is the point where the second spatial derivative of temperature changes its sign. From field aligned simulations, it has been shown that such change in the sign, occurs at a position along the loop where the temperature is approximately 0.6 times the temperature at loop apex (Klimchuk et al. 2008). Cargill et al. (2012b) included additional physics such as gravitational stratification and corrections in the radiative cooling phase, for studying the evolution of single fluid plasma in loops, in the 0D description developed in Klimchuk et al. (2008). The version of single-fluid EBTEL used in Cargill et al. (2012b) will be referred to as EBTEL2 throughout. The results obtained using EBTEL2 show remarkable agreement with those obtained from the field aligned simulations performed with state-of-the-art HYDRADynamics and RADiation (HYDRAD) (Bradshaw & Mason 2003; Bradshaw & Cargill 2006) code and differ at most by 15–20% (Cargill et al. 2012b).

One of the crucial assumptions made in EBTEL and EBTEL2 is that at all stages of the loop evolution, the flows are subsonic. Therefore, the kinetic energy term is neglected from the Navier-Stokes equation. The assumption is consistent with results from field aligned simulations performed using wide range of loop length and heating function. However in cases where HYDRAD predicts subsonic flows, EBTEL2 may compute Mach numbers close to, or even exceeding unity. This is a consequence of neglecting the kinetic energy, which becomes relevant during the impulsive phase of evolution of loop in these cases. Mach numbers exceeding unity in reality would lead to shocks and disrupt flows by converting kinetic energy into heat. In such situations, a simplified 0D description becomes inadequate. Therefore, it is necessary to include the kinetic energy term in the Navier-Stokes equation to be able to study the dynamics of the loop. This is the main aim of this paper.

It is important to point out that the Mach numbers generated by field aligned codes can also reach values close to or exceeding unity. Note that while field aligned codes such as HYDRAD have the potential to tackle shocks, that is not the case for 0D codes such as EBTEL. Nevertheless, despite the simplified nature of 0D calculations, the computed temperature, density, and pressure are in reasonable agreement with field aligned simulations performed using HYDRAD.

The rest of the paper is structured as follows. In § 2 we describe the 0D description of coronal loops, first neglecting kinetic energy in § 2.1, and then including it in § 2.2. We discuss the results for a particular exemplar case. The 0D code based on modified equations derived in § 2.2 is referred to as EBTEL2+KE. We compare these results with those obtained using EBTEL2 as well as using field aligned solution from HYDRAD. In § 2.3, we discuss the validity of approximations used in § 2.2, describe their shortcomings, improve upon these approximations, and demonstrate their validity. All the changes discussed in § 2.2 and 2.3 are incorporated in a newer version of the code, EBTEL3. In § 3.1-3.6 we show the results obtained from EBTEL3 for various cases, covering wide range of loop length, heating function, and Mach numbers at coronal base. These have been compared with results obtained from EBTEL2 and HYDRAD. We also investigate the parameter space where the simulated 0D Mach numbers are unreliable and develop a heuristic way to identify such instances in § 3.7. Finally, we summarize our work in § 4.

## 2. EBTEL FRAMEWORK

The 0D description of coronal loops requires integrating the field aligned hydrodynamical equations over the corona and the transition region. We first describe the field aligned equations in brief.

The Navier Stokes equation for inviscid fluid for high temperature plasma filling a magnetic flux tube is,

$$\frac{\partial}{\partial t} \left( \frac{1}{\gamma-1} P + \frac{1}{2} n \mu v^2 \right) = - \frac{\partial}{\partial s} \left( \left[ \frac{\gamma}{\gamma-1} P + \frac{1}{2} n \mu v^2 \right] v + F \right) + Q - n^2 \Lambda(T) + n \mu g_{\parallel} v, \quad (1)$$

where  $t$  denotes time,  $s$  denotes field aligned loop coordinate,  $P$  is pressure,  $\gamma$  is the polytropic index,  $v$  is velocity,  $\mu$  is the effective ion mass,  $n$  is the electron number density,  $Q$  is the heating rate per unit volume,  $F$  is the heat flux,  $\Lambda(T)$  is the optically thin power loss function,  $T$  is the temperature, and  $g_{\parallel}$  is the component of acceleration due to gravity along the direction of the magnetic field (see e.g. Klimchuk et al. 2008).

The equation of motion is,

$$\frac{\partial v}{\partial t} + v \frac{\partial v}{\partial s} = - \frac{1}{n \mu} \frac{\partial P}{\partial s} + g_{\parallel}, \quad (2)$$

and the equation governing conservation of mass is,

$$\frac{\partial n}{\partial t} + \frac{\partial J}{\partial s} = 0 \quad (3)$$

where  $J$  is the electron flux.

These equations are closed by an equation of state which in this case is the ideal gas law  $P = 2nk_B T$ , where  $k_B$  is the Boltzmann constant. The factor of 2 is because the plasma is assumed to be fully ionized hydrogen plasma. While  $P$  refers to total pressure of ions and electrons,  $n$  is number density of electrons.

2.1. 0D equations for subsonic flows

Klimchuk et al. (2008) derived the 0D equations for subsonic flows by neglecting the kinetic energy term ( $\frac{1}{2}n\mu v^2 \ll P$ ) in a symmetric loop with a uniform cross section. Due to symmetry, the vector quantities, *viz.* heat flux, electron number density flux, and velocity vanish at the loop apex.

On integrating equation 1 under the assumption of subsonic flows, from the coronal base of the loop ( $s = 0$ ) to the loop apex ( $s = L$ ), we find

$$\frac{1}{\gamma - 1} L \frac{d\bar{P}}{dt} = \frac{\gamma}{\gamma - 1} P_0 v_0 + F_0 + \bar{Q}L - \bar{n}^2 \Lambda(\bar{T})L, \quad (4)$$

where  $\bar{P}$ ,  $\bar{n}$ ,  $\bar{T}$  and  $\bar{Q}$  denote the pressure, electron number density, temperature, and heating rate per unit volume, averaged over the coronal part of the loop respectively.  $P_0$  and  $v_0$  are the pressure and velocity respectively at the coronal base.  $F_0$  is the heat flux across  $s = 0$ .

The heat flux is due to particles in the thermal pool. This is a combination of Spitzer flux accounting for Coulomb collisions, and saturation flux that corrects for over-prediction of the heat flux by classical expression (see Klimchuk et al. 2008). However, a significant fraction of energy can also be carried away by non-thermal electrons. The effect of the latter can be readily included as discussed in Klimchuk et al. (2008). For this purpose, flux of non-thermal electrons across coronal base ( $J_{nt0}$ ) and average energy per non-thermal electron ( $E_{nt}$ ) need to be given as additional inputs. Under such a scenario,  $F_0$  is the sum of the thermal conduction flux ( $F_{t0}$ ) and the energy flux carried by non-thermal electrons ( $E_{nt}J_{nt0}$ ), across the coronal base. Similarly  $J_0$  becomes the sum of flux of electrons in the thermal pool ( $n_0 v_0$ ), and non-thermal electrons ( $J_{nt0}$ ), across the coronal base.

On integrating equation 1 for subsonic flows, from the base of the part of loop in transition region ( $s = -l$ ) to the coronal base of the loop ( $s = 0$ ), we find

$$\frac{1}{\gamma - 1} l \frac{d\bar{P}_{tr}}{dt} \approx 0 = -\frac{\gamma}{\gamma - 1} P_0 v_0 - F_0 + l\bar{Q} - c_1 \bar{n}^2 \Lambda(\bar{T})L, \quad (5)$$

where  $\bar{P}_{tr}$  is the average pressure in the transition region, and following Klimchuk et al. (2008) we ignore  $l \frac{d\bar{P}_{tr}}{dt}$  and  $l\bar{Q}$  because of small length of the transition region ( $l$ ).

The quantity  $c_1 \bar{n}^2 \Lambda(\bar{T})L$  is the total radiation loss from transition region, where  $\bar{n}$  is the average electron density in corona (not the transition region). This is  $c_1$  times the total radiation loss from the corona. Based on results from field aligned simulations, it was assumed to be constant in time and equal to 4 in Klimchuk et al. (2008). However Cargill et al. (2012b) dynamically computed it at each time step by including gravitational stratification of corona and corrections in radiative cooling phase, when the loops become over dense as compared to equilibrium value. Both EBTEL2 and enhancement developed in this work (EBTEL3), compute  $c_1$  dynamically at each time step.

Adding equations 4 and 5, we get

$$\frac{1}{\gamma - 1} L \frac{d\bar{P}}{dt} = \bar{Q}L - (1 + c_1) \bar{n}^2 \Lambda(\bar{T})L. \quad (6)$$

On integrating equation 3 from the base of the loop in the corona ( $s = 0$ ) to the top of the loop ( $s = L$ ), we get

$$L \frac{d\bar{n}}{dt} = J_0 = n_0 v_0 = \frac{P_0}{2k_B T_0} v_0, \quad (7)$$

where  $n_0$  is the electron number density at coronal base,  $J_0$  is the flux of electrons across the coronal base ( $s = 0$ ). If there is an additional flux of non-thermal electrons,  $J_0 = \frac{P_0}{2k_B T_0} v_0 + J_{nt0}$ . In either case for expressing  $P_0$  in terms of  $\bar{P}$ , it is assumed that the loop is in hydrostatic equilibrium and is isothermal, with temperature equal to the average coronal temperature, *i.e.*  $[\frac{P_0}{P}] = [\frac{P_0}{P}]_{hse}$ . The subscript *hse* denotes hydrostatic equilibrium and at uniform temperature. The temperature at loop top ( $T_a$ ) is related to  $\bar{T}$  by a constant  $c_2 = 0.9$ , such that  $\frac{\bar{T}}{T_a} = c_2$ . The temperature at coronal base ( $T_0$ ) is related to temperature at loop top ( $T_a$ ) by another constant  $c_3 = 0.6$ , such that  $\frac{T_0}{T_a} = c_3$ .

Finally, the system described by equations. 5, 6, and 7 is closed by the ideal gas law,

$$\bar{P} = 2\bar{n}k_B \bar{T} \quad (8)$$

### 2.2. 0D equations without the assumption of subsonic flows

We now derive the 0D equations that avoid the assumption of subsonic flows in coronal loops. Using equations 2 and 3, we write the time derivative of kinetic energy,

$$\frac{\partial}{\partial t} \left( \frac{1}{2} n \mu v^2 \right) = -\frac{1}{2} \mu v^2 \frac{\partial}{\partial s} (J - nv) - \frac{\partial}{\partial s} \left( \frac{1}{2} n \mu v^3 \right) - v \frac{\partial P}{\partial s} + n \mu v g_{\parallel}. \quad (9)$$

Plugging equation 9 in 1, we obtain

$$\frac{1}{\gamma - 1} \frac{\partial P}{\partial t} = \frac{1}{2} \mu v^2 \frac{\partial}{\partial s} (J - nv) + v \frac{\partial P}{\partial s} - \frac{\partial}{\partial s} \left( \frac{\gamma}{\gamma - 1} P v + F \right) + Q - n^2 \Lambda(T). \quad (10)$$

As discussed in § 2.1, we can include the effect of non-thermal electrons by replacing  $J$  with  $nv + J_{nt}$ , and  $F$  with  $F_t + E_{nt} J_{nt}$ . This gives,

$$\frac{1}{\gamma - 1} \frac{\partial P}{\partial t} = \left( \frac{1}{2} \mu v^2 - E_{nt} \right) \frac{\partial}{\partial s} (J_{nt}) + v \frac{\partial P}{\partial s} - \frac{\partial}{\partial s} \left( \frac{\gamma}{\gamma - 1} P v + F_t \right) + Q - n^2 \Lambda(T). \quad (11)$$

Characteristic velocity of  $10^{6-7}$  cm s<sup>-1</sup> in corona gives kinetic energy of an ion ( $\sim \mu v^2$ )  $\approx 10^{-12} - 10^{-10}$  ergs. This is similar to average thermal energy per electron ( $\sim k_B T$ )  $\approx 10^{-10}$  ergs for  $T=1$  MK. For the non-thermal electrons to escape the thermal pool, their average energy should be much larger than the average thermal energy per electron ( $\frac{1}{2} \mu v^2$ ), and hence the above equation 11 can be simplified, as

$$\frac{1}{\gamma - 1} \frac{\partial P}{\partial t} = v \frac{\partial P}{\partial s} - \frac{\partial}{\partial s} \left( \frac{\gamma}{\gamma - 1} P v + F \right) + Q - n^2 \Lambda(T). \quad (12)$$

Integrating equation 12 from the coronal base of the loop ( $s = 0$ ) to the loop apex ( $s = L$ ) we find,

$$\frac{1}{\gamma - 1} L \frac{d\bar{P}}{dt} = \int_0^L v \frac{\partial P}{\partial s} ds + \frac{\gamma}{\gamma - 1} P_0 v_0 + F_0 + \bar{Q}L - \bar{n}^2 \Lambda(\bar{T})L. \quad (13)$$

Similarly on integrating equation 12 from base of part of the loop in the transition region ( $s = -l$ ) to the coronal base of the loop ( $s = 0$ ), we have

$$\frac{1}{\gamma - 1} l \frac{d\bar{P}_{tr}}{dt} \approx 0 = \int_{-l}^0 v \frac{\partial P}{\partial s} ds - \frac{\gamma}{\gamma - 1} P_0 v_0 - F_0 - c_1 \bar{n}^2 \Lambda(\bar{T})L. \quad (14)$$

To solve the integral on the right hand side of equation 14, we first multiply the equation of motion (equation 2) with  $-n\mu v$  throughout and then integrate from  $s = 0$  to  $s = -l$ . This gives us

$$\int_{-l}^0 v \frac{\partial P}{\partial s} ds = - \int_{-l}^0 \left( n \mu v \frac{\partial v}{\partial t} + n \mu v^2 \frac{\partial v}{\partial s} - n \mu v g_{\parallel} \right) ds \approx -\frac{1}{2} n_0 \mu v_0^3. \quad (15)$$

where we have assumed that the transition region is in a steady state, i.e.  $\frac{\partial v}{\partial t} = 0$  and  $nv = n_0 v_0$ . Using estimates of  $g \approx 10^4$  cm s<sup>-2</sup>,  $l \approx 10^7$  cm, and  $v_0 \approx 10^{6-7}$  cm s<sup>-1</sup> (Klimchuk et al. 2008), we find that  $n_0 \mu v_0 g_{\parallel} l$  is negligible in comparison to  $\frac{1}{2} n_0 \mu v_0^3$ .

Using equations 15 in 14 we obtain (see also Priest (2014))

$$0 = -\frac{1}{2} n_0 \mu v_0^3 - \frac{\gamma}{\gamma - 1} P_0 v_0 - F_0 - c_1 \bar{n}^2 \Lambda(\bar{T})L, \quad (16)$$

which refers to the statement of energy balance in transition region. The balance of the first three terms i.e., fluxes of energy (kinetic, enthalpy, and heat) passing between the transition region and corona, is the energy lost by radiation. It has been assumed that any mass and energy flow through the bottom of transition region is negligible. Work done by or against gravity, and direct heating in the thin transition region have also been neglected. However it should be noted that in the presence of a large variation in cross sectional area, the transition region can thicken substantially (Cargill et al. 2021). The kinetic energy term in equation 16 is the only difference from the earlier versions of EBTEL. Note that equation 16 is cubic in  $v_0$ , and can be solved analytically (see appendix A).

Adding equation 16 and equation 13 we get

$$\frac{1}{\gamma-1}L\frac{d\bar{P}}{dt} = -\frac{1}{2}n_0\mu v_0^3 + \int_0^L v\frac{\partial P}{\partial s}ds + \bar{Q}L - (1+c_1)\bar{n}^2\Lambda(\bar{T})L. \quad (17)$$

Field aligned hydrodynamic simulations performed using HYDRAD for benchmarking EBTEL3 show that

$$\int_0^L v\frac{\partial P}{\partial s}ds \approx -\frac{1}{2}n_0\mu v_0^3 \quad (18)$$

holds well during most of the times. It should be noted that this integral under steady state assumption in corona, should have been  $\int_0^L v\frac{\partial P}{\partial s}ds \approx -\int_0^L (n\mu v\frac{\partial v}{\partial t} + n\mu v^2\frac{\partial v}{\partial s} - n\mu v g_{||}) ds \approx \frac{1}{2}n_0\mu v_0^3$ , if the third term was ignorable in the corona as it is in the transition region (see equation 15). This gives us the same magnitude as the expression we use, however the sign is opposite. Plugging this value in equation 17, we obtain

$$\frac{1}{\gamma-1}L\frac{d\bar{P}}{dt} = -n_0\mu v_0^3 + \bar{Q}L - (1+c_1)\bar{n}^2\Lambda(\bar{T})L. \quad (19)$$

The description of system is completed by equations 7 and 8.

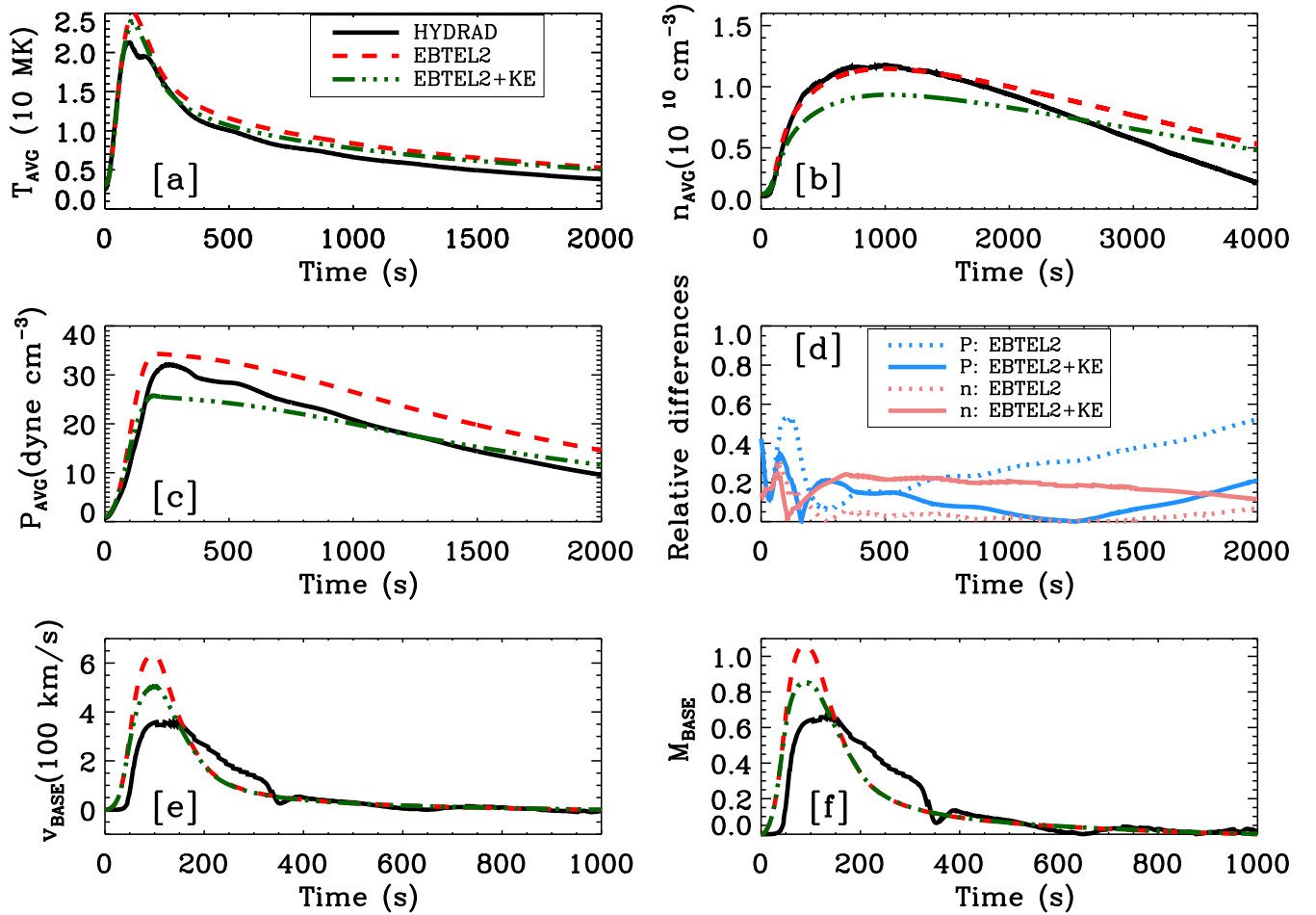


**Figure 1.** Simulation results for the exemplar case. The curves demonstrate the time evolution of  $\bar{T}$  (panel [a]),  $\bar{n}$  (panel [b]), and  $\bar{P}$  (panel [c]), the discrepancy in  $\bar{n}$  (red curves) and  $\bar{P}$  (blue curves) between HYDRAD and those calculated from EBTEL2 (dotted) and EBTEL2+KE (solid) (panel [d]), velocity at coronal base of loop ( $v_0$ ) (panel [e]), and corresponding Mach number ( $M_0$ ) (panel [f]).

In order to test the results obtained by equations 7, 8, 16, and 19, we consider an exemplar case which generates supersonic flows in EBTEL2 and subsonic flows in HYDRAD. This serves as a useful test for simulations performed using the system of modified equations 7, 8, 16, and 19, which are collectively labeled as EBTEL2+KE. We simulate the evolution of a loop of half length 65 Mm, with background heating adjusted such that the initial density and temperature are  $11.05 \times 10^8 \text{ cm}^{-3}$  and 2.51 MK, respectively. The system is subjected to a symmetric triangular heating profile lasting for 200 s, with the maximum heating rate being  $0.5 \text{ ergs cm}^{-3} \text{ s}^{-1}$  at  $t = 100 \text{ s}$ . This corresponds to energy deposition of  $3.25 \times 10^{11} \text{ ergs cm}^{-2}$  in 200 s.

The results of this test case are shown in Figure 1, with simulations from HYDRAD (solid black curves), EBTEL2 (dashed red curves), and EBTEL2+KE (dash-triple-dotted green curves). Following Cargill et al. (2012b) and Klimchuk et al. (2008), we have identified the coronal part of the loop in HYDRAD as the portion where the temperature is greater than or equal to 0.6 times the temperature at loop top. Pressure, density, and temperature have been averaged over this region to obtain coronal averages. The lowest point of this region is taken as the coronal base, where velocity and Mach number have been evaluated. The apex quantities have been obtained by HYDRAD, averaging over the top 20% of the length of the loop.

Figure 1 shows the time evolution of average temperature (panel [a]), the average electron number density (panel [b]), the average pressure (panel [c]). We also plot in panel [d] the absolute relative differences of  $\bar{P}$  and  $\bar{n}$  as computed from EBTEL2 or EBTEL2+KE relative to HYDRAD, which are defined as

$$\frac{\Delta \bar{P}}{\bar{P}} = \left| \frac{\bar{P}_{\text{HYDRAD}} - \bar{P}_{\text{EBTEL2}}}{\bar{P}_{\text{HYDRAD}}} \right| \quad \& \quad \frac{\Delta \bar{n}}{\bar{n}} = \left| \frac{\bar{n}_{\text{HYDRAD}} - \bar{n}_{\text{EBTEL2}}}{\bar{n}_{\text{HYDRAD}}} \right|. \quad (20)$$

In panels [e] and [f], we show the time evolution of velocity and Mach number at coronal base ( $v_0$  and  $M_0$ ) respectively.

We find that the temperatures obtained using EBTEL2 and EBTEL2+KE are nearly identical (panel [a]). The electron number densities obtained with EBTEL2+KE are, however, consistently lower than those obtained with EBTEL2 (panel [b]). However, the relative error remains less than 25 % (see panel [d]). The average pressure plotted in panel [c] shows that the agreement between HYDRAD and EBTEL2+KE is better, except during a small time window close to where pressure peaks. A better agreement for velocity is also seen in HYDRAD and EBTEL2+KE (panel [e]) and Mach number (panel [f]) at the base. While HYDRAD produces subsonic flows at base (panel [f]), EBTEL2 produces Mach numbers exceeding 1. If these are trusted, it should lead to shocks, which cannot be tackled by 0D simulations. The EBTEL2+KE brings down Mach numbers below unity. However, we note that improvements in Mach numbers are unsatisfactory, given the small improvement in velocity and Mach numbers at the cost of deterioration in electron number density. Therefore, further improvements are needed.

### 2.3. Assessment and improvements of the approximations

While seeking solutions to the equations 7, 8, 16, and 19, we have made two approximations, which we now discuss in some details. The first approximation (also present in EBTEL2) is related to the ratio of pressure and electron number density at the coronal base with their average values. EBTEL2 computes the ratio of the pressure at the coronal base and average pressure by assuming the system to be in hydrostatic equilibrium i.e.  $P(s) = P_0 \exp(-s/L_H(\bar{T}))$ . The variation of temperature along the loop is neglected and scale height ( $L_H$ ) is computed using a temperature equal to the coronal average value. Cargill et al. (2012b) discuss that this is equivalent to  $[\frac{P_0}{\bar{P}}]_{hse} = \exp(2L \sin(\frac{\pi}{5})/\pi L_H(\bar{T}))$  for a semicircular loop, where the subscript hse indicates that the loop is in hydrostatic equilibrium at uniform temperature ( $\bar{T}$ ). Using the constants  $\frac{\bar{T}}{T_a} = c_2 = 0.9$  and  $\frac{T_b}{T_a} = c_3 = 0.6$ , the temperature at the coronal base ( $T_0$ ) is 0.67 times the average temperature of loop ( $\bar{T}$ ). Using these along with  $P_0 = 2n_0 k_B T_0$  and  $\bar{P} = 2\bar{n} k_B \bar{T}$ , the ratio of electron number density at the coronal base to its coronal average ,

$$\left[ \frac{n_0}{\bar{n}} \right]_{hse} = \frac{3}{2} \exp(2L \sin(\frac{\pi}{5})/\pi L_H(\bar{T})). \quad (21)$$

To assess this approximations, we define the following two coefficients and compute these using HYDRAD,

$$c_4 = \left[ \frac{P_0}{\bar{P}} \right] \left[ \frac{P_0}{\bar{P}} \right]_{hse}^{-1} \quad \& \quad c_5 = \left[ \frac{n_0}{\bar{n}} \right] \left[ \frac{n_0}{\bar{n}} \right]_{hse}^{-1} \quad (22)$$

We show the evolution of  $c_4$  and  $c_5$  as the solid curves in panels [a] and [b] of Figure 2 respectively. In order to relate the pressure and electron number density at the base of the corona and their averages across the loop, EBTEL2 assumes



a hydrostatic profile, with  $c_4$  and  $c_5$  approximated as constants,  $c_{4A} = 1$  and  $c_{5A} = 1$  respectively; these are shown as dashed lines in Figure 2. These approximation are clearly discrepant by up to factors of 2 during the impulsive phase. Hence, we need to develop a better approximation to relate the base pressure and electron number density to the quantities computed within the EBTEL framework,  $\bar{P}$ ,  $\bar{n}$ ,  $\bar{T}$  and  $v_0$

We attribute the variation of  $c_4$  and  $c_5$  from their constant values of 1, mainly to two aspects: 1) since the plasma is accelerated into the loop, it requires larger pressure gradients than hydrostatic values, in lower parts of loop, 2) since the plasma velocity at apex of the loop is zero, the flow must be decelerated, and therefore the pressure gradient in the upper parts of the loop should be smaller than hydrostatic or perhaps even in the opposite direction. From the plots, it appears that for the first 150 s, the first cause dominates, while the second dominates during the later phase till about 350 s.

To ascertain the validity of our second approximation (equation 18), we compute following two quantities,

$$I = \int_0^L v \frac{\partial P}{\partial s} ds - \frac{1}{2} n_0 \mu v_0^3 \quad (\text{without approximation}) \quad (23)$$

$$I_A = -n_0 \mu v_0^3 \quad (\text{with approximation})$$

using HYDRAD and plot them in panel [c] of figure 2. The reasonable match between the two curves suggests that this approximation is satisfactory, albeit being relatively poor between 150-350 seconds. This could be attributed to the following effects. In the impulsive phase (upto 150 s) in order to fill plasma into the loop, there should be acceleration. Hence dominating contribution to  $I$  should be from portions of loop where force due to pressure gradients ( $-\frac{\partial P}{\partial s}$ ) are in the same direction as the velocity of plasma ( $v$ ). This means pressure gradients are opposite to plasma velocity at locations from where larger contribution to  $I$  comes from. Since our approximation  $I_A$  predicts negative values, it matches well with  $I$  in this duration. However, between 150-350 seconds, the effect of pressure gradients with directions opposite to hydrostatic pressure gradients (for decelerating plasma) becomes more important (see panel [a] of figure 2). Since plasma is being decelerated, larger contribution to  $I$  should come from portions of the loop where pressure force ( $-\frac{\partial P}{\partial s}$ ) is opposite to velocity ( $v$ ). Clearly for such regions pressure gradient is along velocity, but since our approximation  $I_A$  still gives negative values, it introduces errors.

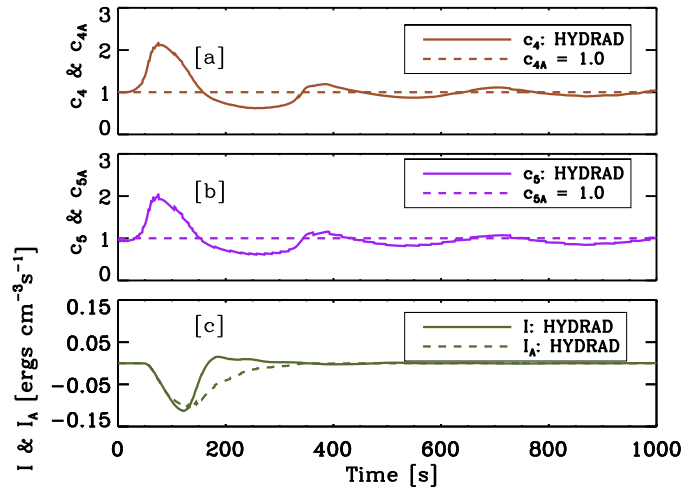


**Figure 2.** Comparing the effects of different approximations within HYDRAD for the exemplar case (see Figure 4). [a] The *top panel* (with brown curves) shows the evolution of the pressure coefficient  $c_4$  (solid curve; equation 22) and the approximation used in EBTEL2,  $c_{4A} = 1$  (dashed line). [b] The *middle pane* (purple curves) shows the evolution of the electron number density coefficient  $c_5$  (solid curve; equation 22) and the approximation used in EBTEL2,  $c_{5A} = 1$  (dashed line). [c] The *bottom panel* (olive curves) shows the evolution of energy flux  $I$  and our approximation  $I_A$  (solid and dashed curves respectively; equation 23), with both  $I$  and  $I_A$  are computed using HYDRAD. Note that the approximations to the pressure and electron number density coefficients  $c_{4A}$  and  $c_{5A}$  are discrepant by factors of up to 2, whereas the energy flux approximation  $I_A$  is adequate.

In order to improve on the first approximation, we first develop insight on the form of pressure at base of corona in terms of quantities computed within the framework of 0D simulations under assumption of steady flow and uniform

temperature ( $\bar{T}$ ) along the loop. While these conditions are certainly not met in the impulsive phase where kinetic energy dominates, the resulting expressions can be generalized.

Assuming a steady flow in equation 2 and combining that with equation 8, we have

$$\frac{1}{P} \frac{\partial P}{\partial s} = \frac{\mu}{2k_B \bar{T}} \left( g_{\parallel} - \frac{1}{2} \frac{\partial v^2}{\partial s} \right) \quad (24)$$

Under the assumption that acceleration due to gravity and any variation in temperature can be neglected, we integrate equation 24 to obtain

$$\frac{P(s)}{P_0} = \exp \left[ \frac{\mu}{2k_B \bar{T}} \left( s g_{\parallel} - \frac{1}{2} (v^2 - v_0^2) \right) \right] = \exp \left[ -\frac{s}{L_H} \right] \exp \left[ \frac{\gamma}{2} (M_0^2 - M^2) \right] \quad (25)$$

where  $M = \sqrt{\frac{\mu v^2}{2\gamma k_B \bar{T}}}$ , and  $L_H = -\frac{2k_B \bar{T}}{\mu g_{\parallel}}$ . The minus sign in  $L_H$  is due to  $g_{\parallel}$  being negative.  $M_0$  denotes Mach number at base  $s = 0$ .

We now convert the above expression into a form which can be used to place bounds on pressure at base of corona in terms of quantities which can be computed within the domain of 0D description of loops, viz. average pressure and Mach number at coronal base. We consider two functions  $X_1$  and  $X_2$  of time and loop length such that for a particular loop of length  $L$ , the minimum and maximum values of  $\exp \left[ -\frac{\gamma}{2} (M_0^2 - M^2) \right]$  at a time are  $\exp [X_1 M_0^2]$  and  $\exp [X_2 M_0^2]$  respectively. Hence, averaging equation 25 over the coronal part of the loop, we obtain

$$\left[ \frac{P_0}{P} \right]_{hse} \exp [X_1 M_0^2] \leq \left[ \frac{P_0}{P} \right] \leq \left[ \frac{P_0}{P} \right]_{hse} \exp [X_2 M_0^2] \quad (26)$$

where  $\left[ \frac{P_0}{P} \right]_{hse}$  is the ratio of base and average pressure, if system was in hydrostatic equilibrium and isothermal with a temperature  $\bar{T}$ , while  $\left[ \frac{P_0}{P} \right]$  is actual value. The expressions in equation 26 is consistent with the fact that in the regime where Mach numbers approach 0, we will recover the hydrostatic expression.

Without any loss of generality, we can express the ratio  $\left[ \frac{P_0}{P} \right]$  and  $\left[ \frac{n_0}{n} \right]$

$$\left[ \frac{P_0}{P} \right] = \left[ \frac{P_0}{P} \right]_{hse} \exp[\phi(t, L) M_0^2] \quad \& \quad \left[ \frac{n_0}{n} \right] = \left[ \frac{n_0}{n} \right]_{hse} \exp[\phi(t, L) M_0^2] \quad (27)$$

where  $\phi$  is a function of time and loop length. Moreover, for a particular loop at a time  $t$ , it is bounded by the relation  $X_1 \leq \phi \leq X_2$ . Even though we arrived at equation 27 assuming steady flow in an isothermal loop, one can always invert it to express  $\phi(t, L)$  at each time step in terms of  $\left[ \frac{P_0}{P} \right]$ , and  $\left[ \frac{P_0}{P} \right]_{hse}$ , for the general case of non-steady flows in multi-thermal loops. However, it is infeasible to derive an exact expression for  $\phi(t, L)$  as it would require a field aligned simulation in the first place to be computed. Therefore, we approximate it as a constant in time, independent of loop length. We compared the results between HYDRAD and EBTEL for different values of  $\phi$  while also comparing  $c_4$  and  $c_5$  with the new code. We compute again the approximations  $c_{4A}$  and  $c_{5A}$  to coefficients  $c_4$  and  $c_5$  using the expressions

$$c_{4A} = \exp\left[\frac{3}{2} M_0^2\right] \quad \& \quad c_{5A} = \exp\left[\frac{3}{2} M_0^2\right] \quad (28)$$

We find that the calculations are not sensitive to the precise value adopted and choose  $\phi = \frac{3}{2}$ . See Figure 3 for a comparison showing the effect of adopting this nominal value in HYDRAD.

We plot  $c_{4A}$  and  $c_{5A}$  in panels [a] and [b] of Figure 3 using brown dashed ( $c_{4A}$ ) and purple dashed ( $c_{5A}$ ) lines. For comparison we have also plotted  $c_4$  and  $c_5$  computed by HYDRAD using solid lines. The plots reveal that the new approximations on  $c_4$  and  $c_5$  resulting into  $c_{4A}$  and  $c_{5A}$ , respectively, shows the most prominent peak observed during the impulsive phase, albeit at slightly later stage. Furthermore, other peaks occurring in  $c_4$  and  $c_5$  during the later phase of the evolution are also close to the values of  $c_{4A}$  and  $c_{5A}$  in the limit  $M_0 \rightarrow 0$ . However, the prominent dips observed in  $c_4$  and  $c_5$  between 150 and 350 sec are not captured by  $c_{4A}$  and  $c_{5A}$ . We have analyzed these shortcomings and found that the errors due to these are rather small because of decent match between profiles of  $\bar{P}$ ,  $\bar{n}$ ,  $\bar{T}$  and  $v_0$ , computed from field aligned and 0D simulations for different cases considered (see § 3 and Figure 4).

We stress that the resultant expressions in equation 28 are crude, because approximating  $\phi(t, L)$  in equation 27 with a constant value of  $\frac{3}{2}$  does not capture its complicated variation with time and loop length. However, it achieves the twin goals of capturing the most prominent feature (the first peak) of  $c_4$  and  $c_5$  computed from HYDRAD and improving



results of 0D simulations over wide range of parameter space of solar coronal loops as long as the flows in HYDRAD are subsonic.

Finally, using the above described approximations, we simulate the plasma dynamics of the monolithic loop that is discussed in §2.2 and plot the obtained results in Figure 4. We denote the results obtained using the above-described approximations, including the addition of KE, with EBTEL3. For comparison we have plotted the results obtained from HYDRAD (black-solid) as well as EBTEL2 (red-dashed). The results show that temperature (see panel [a]) produced by EBTEL2 and EBTEL3 are still almost overlapping. However both density and pressure are lower in EBTEL3 than EBTEL2. The density derived using EBTEL2, however, is better matched with HYDRAD than that derived with EBTEL3 (see panel [b]). This discrepancy is partially due to the errors in  $c_{4A}$  and  $c_{5A}$ . However, pressure is better reproduced using EBTEL3 (see panel [c]). We plot the velocities and Mach numbers measured at the base of the corona in panels [e] and [f], respectively, that clearly show that EBTEL3 performs better than EBTEL2. Though EBTEL2 predicts Mach numbers exceeding unity, EBTEL3 manages to bring it down to values predicted by HYDRAD. We plot the relative errors in average pressure and electron number density in panel [d]. We find that the deterioration in density due to our approximation over EBTEL2 is less than the improvement in pressure.

#### 2.4. Density computed by EBTEL2 and EBTEL3

The question remains, however, as to why EBTEL2 does a better job than EBTEL3 in predicting the average density when compared to HYDRAD, even when the predicted velocity at the coronal base shows substantial discrepancy. This may be explained as follows. During the impulsive phase, conductive losses dominate and radiative losses are negligible (see also Rajhans et al. 2021; Subramanian et al. 2018; Cargill et al. 1995). Therefore, the sum of enthalpy and kinetic energy flux across coronal base  $\left(\frac{\gamma}{\gamma-1}P_0v_0 + \frac{1}{2}\mu n_0v_0^2\right)$  is approximately equal to the conduction flux ( $F_0$ ) across it. This approximate equality can be used in addition to equation 8 to write the mass flux across coronal base as

$$\mu n_0v_0 = -\frac{F_0}{\frac{2\gamma k_B T_0}{\mu(\gamma-1)} + \frac{v_0^2}{2}} \quad (29)$$

We now look at the quantities involved in this equation namely temperature, conduction flux, and velocity. The temperature estimated by EBTEL2 as well as EBTEL3 are higher than those obtained using HYDRAD, which is due to conduction flux being under-estimated in EBTEL2 and EBTEL3. Hence a lower magnitude of  $F_0$  in EBTEL2 and EBTEL3 than HYDRAD will tend to make magnitude of  $\mu n_0v_0$  lower in EBTEL2 and EBTEL3 than HYDRAD. Additionally an overestimated temperature  $T_0$  in EBTEL2 and EBTEL3 will tend to make magnitude of  $\mu n_0v_0$  lower than those obtained from HYDRAD. However the neglect of kinetic energy ( $\propto \frac{v_0^2}{2}$ ) in EBTEL2 will tend to make the magnitude of mass flux higher than HYDRAD. This is not the case with EBTEL3. This last effect is by far the most important contributor to the discrepancy between mass flux in EBTEL2 and HYDRAD. The mass flux hence obtained from EBTEL3 agrees better with HYDRAD.

However, neither EBTEL2 nor EBTEL3 take into account the dynamic change in the length of the coronal part of the loop. Both assume that the whole loop is in the corona. To compare the EBTEL2 or EBTEL3 results, the coronal portion of loops in HYDRAD is defined dynamically by measuring the length of the part of the loop with temperature  $\geq 0.6T_a$ . Due to this definition, the coronal portion of the loop identified by HYDRAD could be significantly smaller than the full length of the loop considered by EBTEL2 and EBTEL3 in the impulsive phase. This is consistent with the requirement of larger temperature gradients to transfer larger conduction flux to the transition region. The error caused by using larger length of coronal part in equation 7 tends to compensate the higher mass flux in EBTEL2. As a result,  $\bar{n}$  computed by EBTEL2 and HYDRAD match well. The improvement in velocity in EBTEL3 brings the mass flux computed by EBTEL3 closer to that by HYDRAD, but the error caused by taking fixed  $L$  in equation 7 is not canceled sufficiently. This leads to worsening of densities in EBTEL3 than EBTEL2. However, we emphasize that the worsening in densities is significantly smaller than the improvement in pressure and velocity, in terms of agreement with results from HYDRAD.

### 3. RESULTS

Having tested the approximations for a nominal example case, we next carry out a systematic verification covering a useful range of the parameter space of solar coronal loops. All the heating functions have a symmetric triangular profile. The results are compared with those from EBTEL2 and HYDRAD. Table 1 provides the details of the test cases

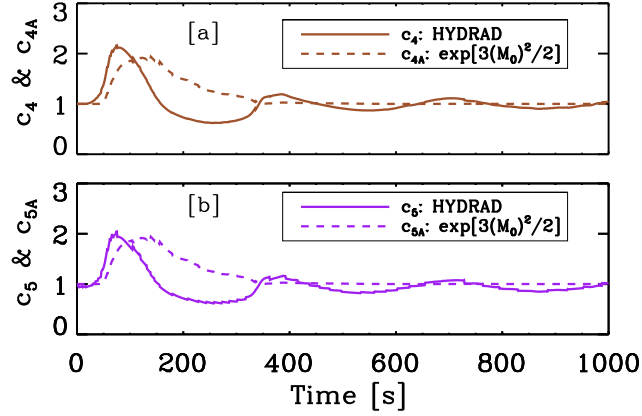


**Figure 3.** As in panels [a] and [b] of Figure 2, but comparing the HYDRAD pressure and electron number density coefficients  $c_4$  and  $c_5$  (solid curves) with approximations made as  $[\exp(\frac{3}{2}M_0^2)]$  (dashed curves; see equation 28) where the Mach number at the base of the corona,  $M_0$ , is computed via HYDRAD. Note that the modifications offer a qualitative improvement in the approximations.

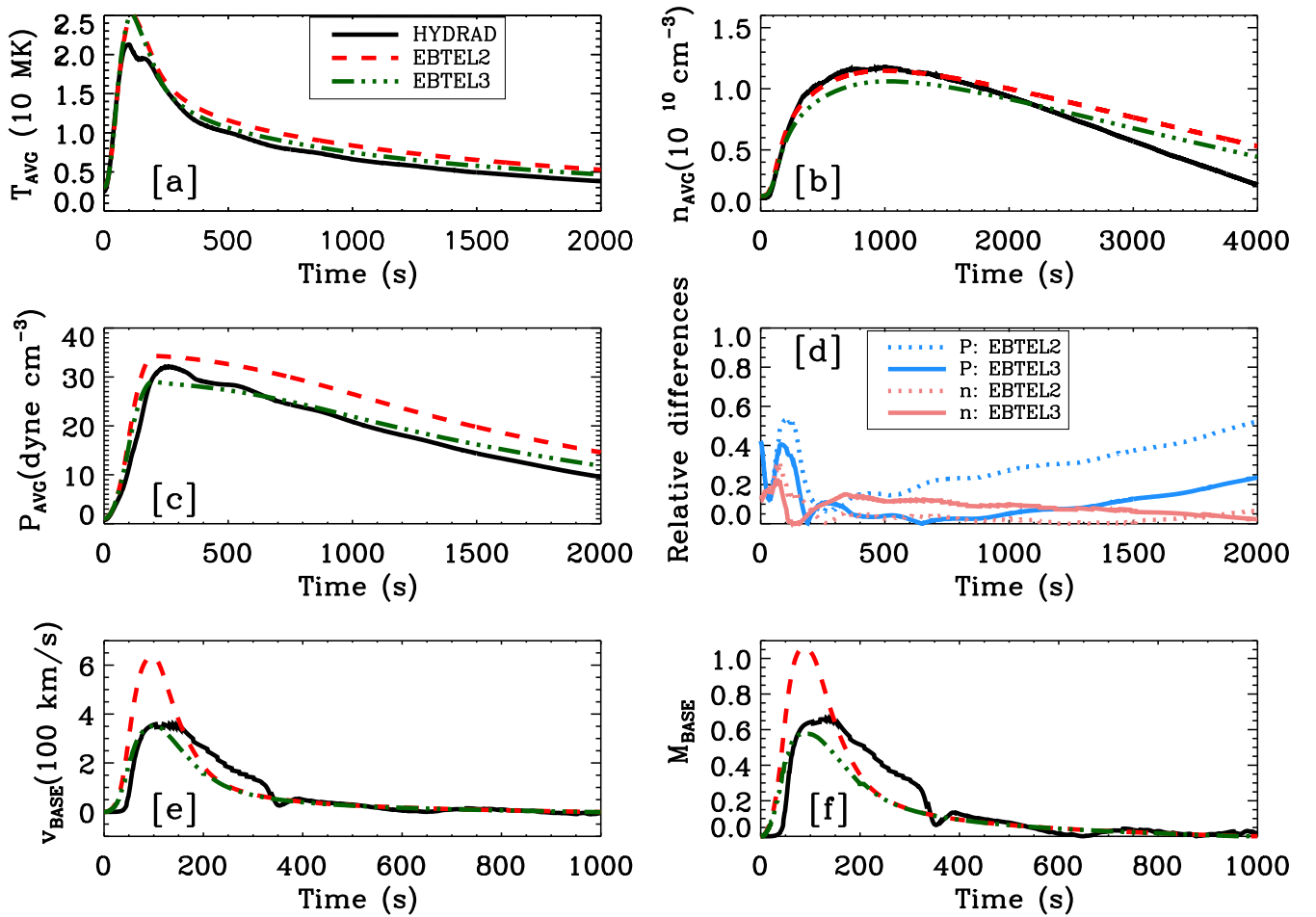


**Figure 4.** As in Figure 1 but with over-plotted green curves obtained with EBTEL3.

chosen for simulations. For the sake of completeness we have also provided in the same table, input parameters for case 1 which was discussed in §2.2 and §2.3. Note that the test cases are chosen such that they cover a wide range of loop lengths, heating functions and the maximum velocities reached in HYDRAD at coronal base cover the regimes of subsonic (cases 1-4), trans-sonic case (5-6) and supersonic (case 7) flows. The maximum Mach numbers achieved at base ( $M_0$ ) in HYDRAD simulations are also listed in table 1. We discuss the results from all the test cases one by one below.

**Table 1.** Simulation parameters such as peak heating rate (2nd column), duration of heating (3rd column), loop half length (4th column), initial electron number density (5th column), initial temperature (6th column), maximum Mach numbers at coronal base computed by HYDRAD (7th column), EBTEL2 (8th column) and EBTEL3 (9th column) for various test cases.

Index	Peak heating rate	Duration of heating	Half Length	Initial $\bar{n}$	Initial $\bar{T}$	$(M_0)_{max}$		
	[ergs cm <sup>-3</sup> s <sup>-1</sup> ]					[s]	[10 <sup>8</sup> cm]	[10 <sup>8</sup> cm <sup>-3</sup> ]
1	0.5	200.0	65.0	11.05	2.51	0.67	1.10	0.58
2	$1.5 \times 10^{-3}$	500.0	75.0	0.62	0.85	0.57	0.88	0.50
3	$1.0 \times 10^{-2}$	200.0	25.0	2.46	0.73	0.49	0.61	0.42
4	2.0	200.0	25.0	22.32	2.06	0.55	0.81	0.51
5	$1.0 \times 10^{-2}$	200.0	50.0	0.84	0.71	0.75	1.32	0.63
6	$1.5 \times 10^{-2}$	200.0	75.0	0.80	0.92	0.94	1.46	0.65
7	$1.0 \times 10^{-3}$	200.0	60.0	0.13	0.42	1.15	1.51	0.65

### 3.1. Case 2

We simulate the plasma dynamics in a loop of half length of 75 Mm with background heating adjusted such that the initial electron number density and temperature are  $0.62 \times 10^8 \text{ cm}^{-3}$  and 0.85 MK, respectively. We provide a symmetric triangular heating profile lasting for 500 s, with the maximum heating rate being  $0.0015 \text{ ergs cm}^{-3} \text{ s}^{-1}$  at  $t = 250 \text{ s}$ .

The results are plotted in Figure 5. As for the first case described above, there is little difference in the temperature profile (panel a), but the electron number density (panel b) is underestimated using EBTEL3 in comparison with that from EBTEL2 and the match with HYDRAD deteriorates. Similar to the underestimation of electron number density, pressure is also underestimated with EBTEL3 and shows better correspondence with the results from HYDRAD. The relative errors in electron number density and pressure obtained by EBTEL3 and EBTEL2 are also plotted in panel [d]. Similar to the case 1, we note that the deterioration in the electron number density due to approximation in EBTEL3 is smaller than the improvements seen in pressure.

The velocity and the Mach number estimated at the base of the corona, both are lower in simulations using EBTEL3 in comparison to EBTEL2 and are in excellent agreement with those obtained with HYDRAD. This is a sub-sonic case, where both EBTEL2 and HYDRAD produce Mach numbers at the base lower than 1.

### 3.2. Case 3

The third case simulates the plasma dynamics in a loop of half length of 25 Mm. The background heating is adjusted such that the initial electron number density and temperature are  $2.46 \times 10^8 \text{ cm}^{-3}$  and 0.73 MK respectively. We provide a symmetric triangular heating profile lasting for 200 s, with the maximum heating rate being  $0.01 \text{ ergs cm}^{-3} \text{ s}^{-1}$  at  $t = 100 \text{ s}$ . We plot the results in figure 6. As before, pressure, velocity and Mach number show significant improvements compared with EBTEL2.

### 3.3. Case 4

Here we take a loop of half length of 25 Mm with background heating adjusted such that the initial electron number density and temperature are  $22.32 \times 10^8 \text{ cm}^{-3}$  and 2.06 MK respectively. We provide a symmetric triangular heating profile lasting for 200 s, with the maximum heating rate being  $2.0 \text{ ergs cm}^{-3} \text{ s}^{-1}$  at  $t = 100 \text{ s}$ . The results are shown in Figure 7. The temperature, electron number density and, pressure show similar evolution as in the other examples described above. The velocity and Mach number plots shown in panel [e] and [f] shows remarkable improvements in EBTEL3 over EBTEL2 when compared with HYDRAD.

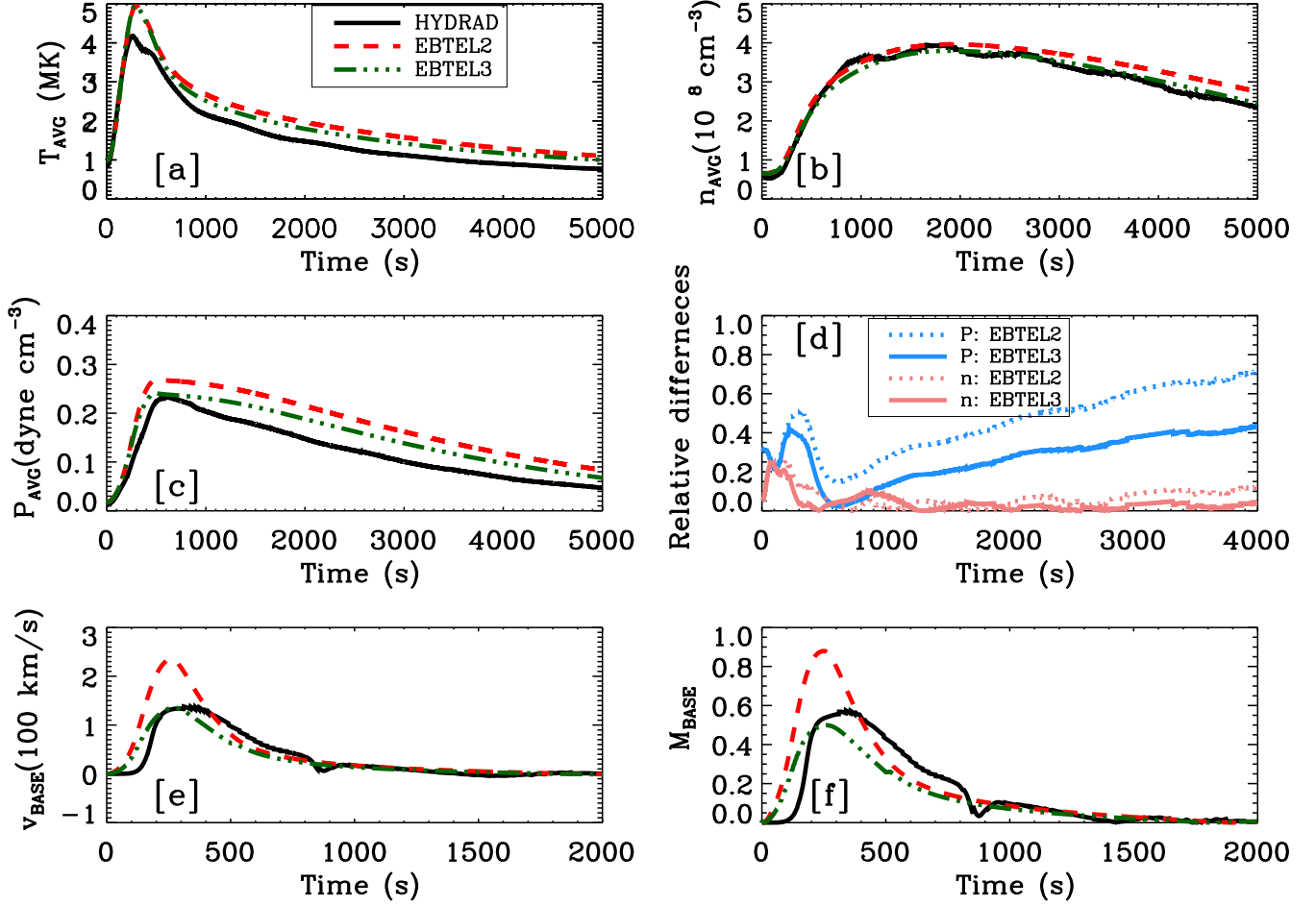


Figure 5. As in Figure 4 but for Case 2: A 75 Mm loop receiving  $2.8125 \times 10^9$  ergs  $\text{cm}^{-2}$  in 500 s.

### 3.4. Case 5

Here we consider a loop of half length of 50 Mm with initial electron number density and temperature are  $0.84 \times 10^8 \text{ cm}^{-3}$  and 0.71 MK. The heating profile lasting for 200 s, with the maximum heating rate being  $0.01 \text{ ergs cm}^{-3} \text{ s}^{-1}$  at  $t = 100$  s. We plot the results in Figure 8. Panel [a] shows the temperature produced by EBTEL2 and EBTEL3 are not overestimated but in close agreement with HYDRAD. This is because in this case, even though velocities at base remain subsonic through out, velocities produced by HYDRAD at intermediate positions in the loop reach supersonic velocities, which leads to shocks and hence dissipation of kinetic energy. This adds to temperature produced by HYDRAD. Since 0D description cannot incorporate the physics of shocks, there is no increase in temperature due to dissipation of kinetic energy. Panels [b]-[d] show similar trends in electron number density and pressure as in previous cases. Panel [e] and [f] show the velocity and Mach number at coronal base respectively. The maximum Mach numbers produced at base of corona in HYDRAD simulations is 0.75 and those produced by EBTEL3 are  $\approx 0.63$ . Mach number produced in EBTEL2 are supersonic  $\approx 1.4$ . The match between Mach numbers computed using HYDRAD and EBTEL3 is worse than previous cases.

### 3.5. Case 6

The sixth case is of a loop of half length of 75 Mm with initial electron number density and temperature are  $0.80 \times 10^8 \text{ cm}^{-3}$  and 0.92 MK. The heating profile lasting for 200 s, with the maximum heating rate being  $0.015 \text{ ergs cm}^{-3} \text{ s}^{-1}$  at  $t = 100$  s. The results are shown in Figure 9. HYDRAD in this case predicts higher temperature than EBTEL, due to dissipation of kinetic energy by shocks in HYDRAD (see panel [a]). We observe the same pattern in the time evolution of electron number density and pressure (see panels [b]-[d]). Panel [e] and [f] show the velocity and

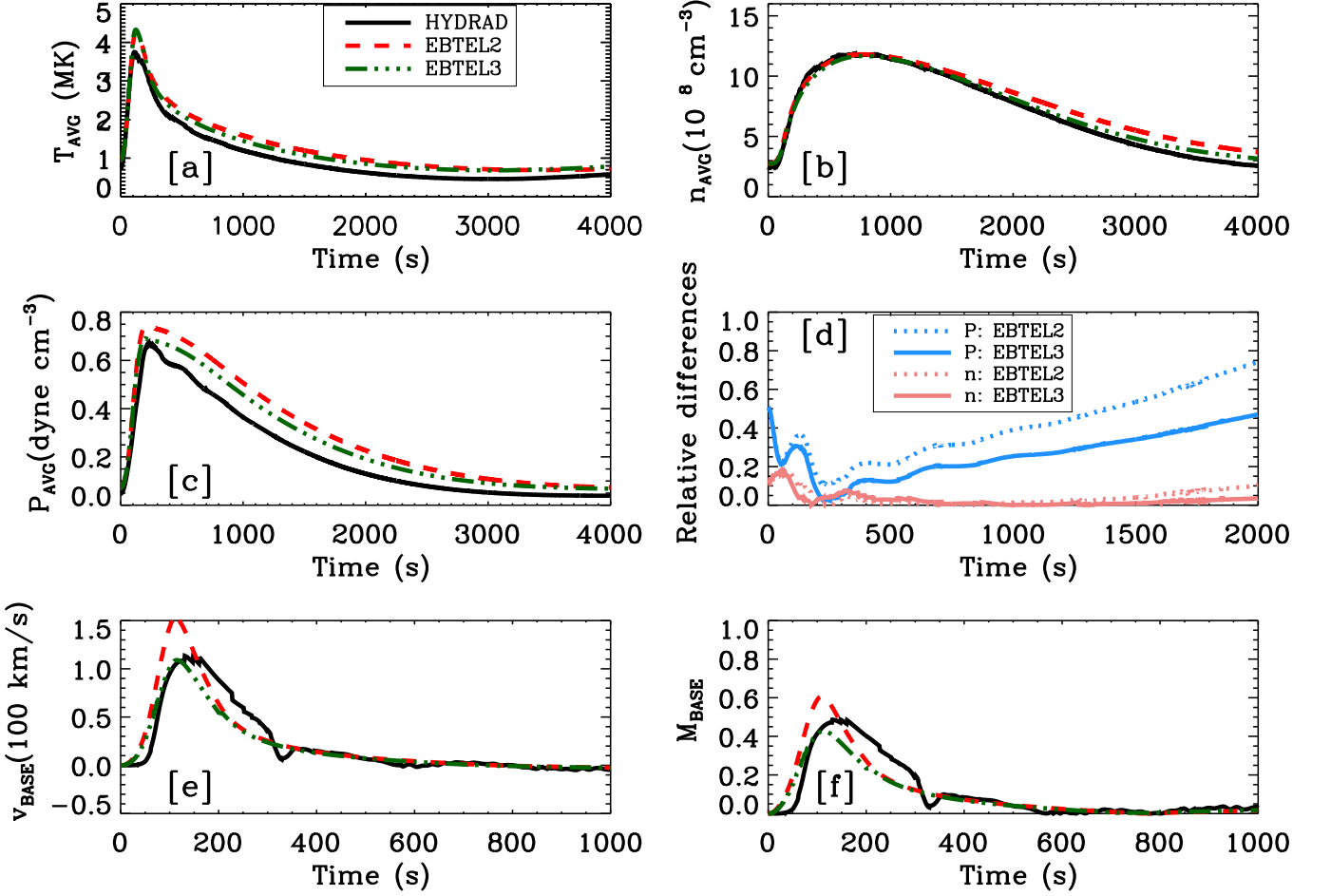


Figure 6. As in figure 4 but for Case 3: A 25 Mm loop receiving  $2.5 \times 10^9$  ergs  $\text{cm}^{-2}$  in 200 s.

Mach number at coronal base of loop. In this case, HYDRAD predicts maximum Mach number of 0.94 while EBTEL2 and EBTEL3 predicts maximum Mach numbers of 1.5 and 0.65, respectively. Though the Mach numbers produced by EBTEL3 are unreliable because of being significantly lower than HYDRAD, the agreement between velocities is better.

Interestingly the agreement between velocity predicted by EBTEL3 and HYDRAD is worse in this case than the previous cases where maximum Mach number at coronal base was well below 1. This worsening of velocity computed by EBTEL3 can be understood as follows. Shocks are formed from the abrupt slowing of a supersonic evaporative upflow. The discontinuous decrease in velocity with height is accompanied by a discontinuous increase in the density. Clearly,  $\frac{n_0}{n}$  must be higher without the shock than with it. Consequently equation 28 gives higher values of  $n_0$  in EBTEL3. The over estimation of  $n_0$  in equation 16 leads to a lower value of  $v_0$ .

### 3.6. Case 7

The seventh case is of a loop of half length of 60 Mm with background adjusted such that the initial electron number density and temperature are  $0.13 \times 10^8 \text{ cm}^{-3}$  and 0.42 MK. It receives a symmetric triangular heating profile lasting for 200 s, with the maximum heating rate being  $0.001 \text{ ergs cm}^{-3} \text{ s}^{-1}$  at  $t = 100$  s. The results are plotted in Figure 9.

In this case, maximum Mach numbers reached by by HYDRAD exceed unity (1.15) at the base. The maximum Mach numbers produced by EBTEL2 and EBTEL3 are 1.51 and 0.65 respectively and both are not reliable because 0D simulations cannot handle shocks, which are expected to occur in reality. Despite this, we see that temperature (panel [a]), density (panel [b]), and pressure (panel [c]) computed from 0D simulations being reliable. As discussed in § 3.5, HYDRAD computes higher temperatures than EBTEL2 and EBTEL3 (see panel [a] of Figure 10). Panel [e] shows that

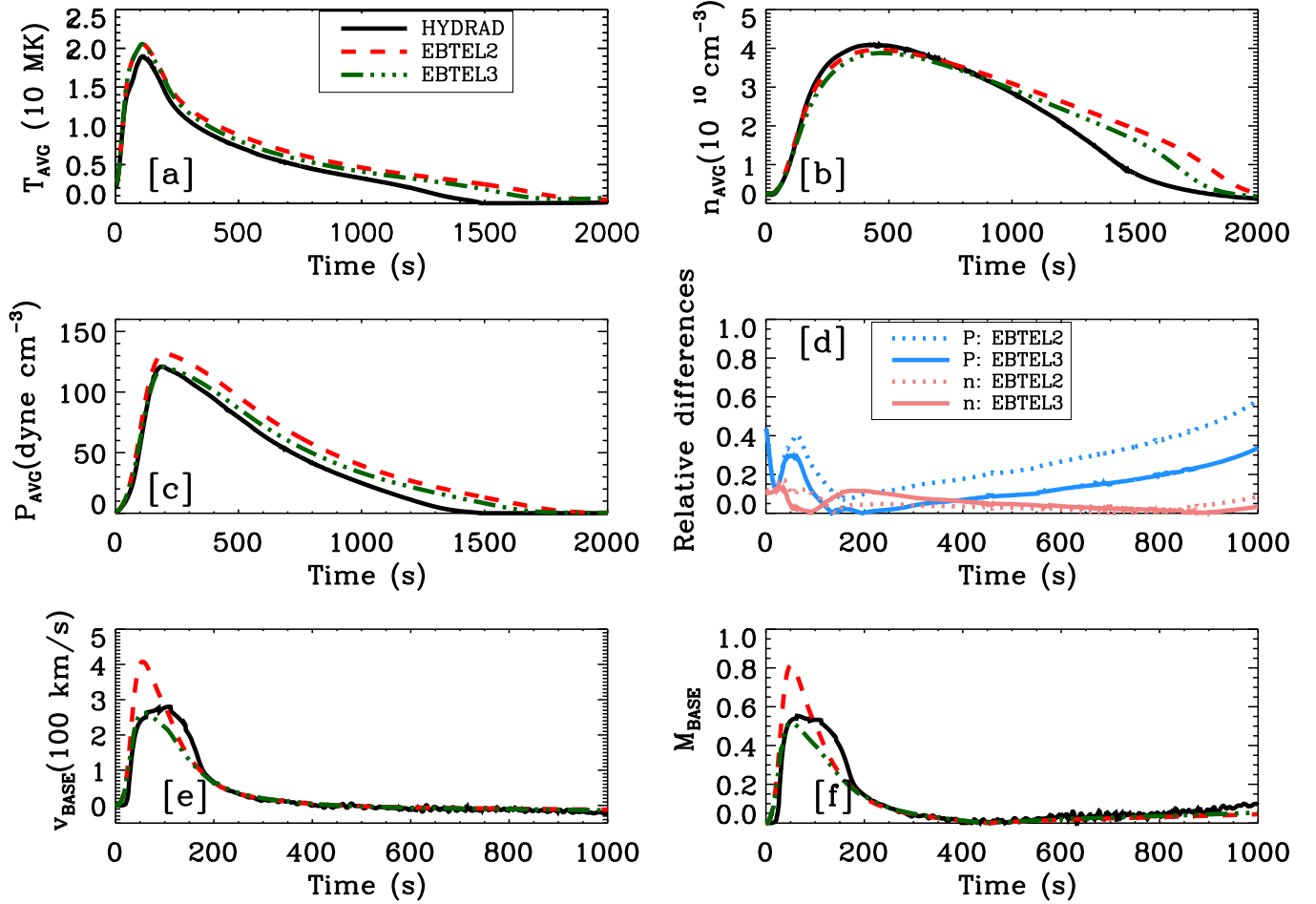


Figure 7. As in Figure 4 but for Case 4: A 25 Mm loop receiving  $5.0 \times 10^{11}$  ergs  $\text{cm}^{-2}$  in 200 s.

EBTEL3 under estimates velocities at coronal base. Even though the peak velocities computed by HYDRAD match better with EBTEL3 than EBTEL2, the Mach numbers computed by EBTEL3 are subsonic and hence cannot be trusted.

### 3.7. Prediction of onset of shocks

From the simulations performed with EBTEL2, EBTEL3, and HYDRAD for various input parameters, we find reasonable agreement between  $\bar{P}$ ,  $\bar{n}$ , and  $\bar{T}$  obtained from HYDRAD and EBTEL3. The agreement for  $v_0$  and  $M_0$  is better when maximum  $M_0$  produced in HYDRAD is subsonic, but starts worsening when  $M_0$  starts approaching or exceeding unity. Despite this, we find that both EBTEL2 and EBTEL3 generate values of  $\bar{P}$ ,  $\bar{n}$ , and  $\bar{T}$  within a factor  $2 \times$  that from HYDRAD. While EBTEL2 provides better  $\bar{n}$ , EBTEL3 provides better  $\bar{P}$ . Additionally EBTEL3 does better for velocities. Note however that the match between  $M_0$  computed from HYDRAD and EBTEL3 is not acceptable in the last two cases, where the maximum  $M_0$  produced in HYDRAD is  $\gtrsim 1$ , but EBTEL3 produces subsonic flows (see table. 1). This is because such  $M_0$  in HYDRAD would lead to shocks, which cannot be modeled by a simple 0D description of loops. Consequently this may lead to the erroneous conclusion that flows in the loop are subsonic. However, we note that even in these cases, 0D is still sufficient to study the electron number density, temperature and pressure as they are not affected as shown in Figures 9 and 10. This is consistent with qualitative arguments made in Cargill et al. (2012a).

In light of above arguments it becomes necessary to be able to use results from 0D simulations for predicting regimes where the maximum  $M_0$  produced in field aligned simulations is  $\gtrsim 1$ . In such cases detailed field aligned hydrodynamical simulations are better suited to compute reliable Mach numbers.

Based on the EBTEL3 simulations, we find a simple criterion that can be employed to predict this regime. A measurement of the ratio of full width at half maximum (FWHM) of the Mach number profile predicted by EBTEL3



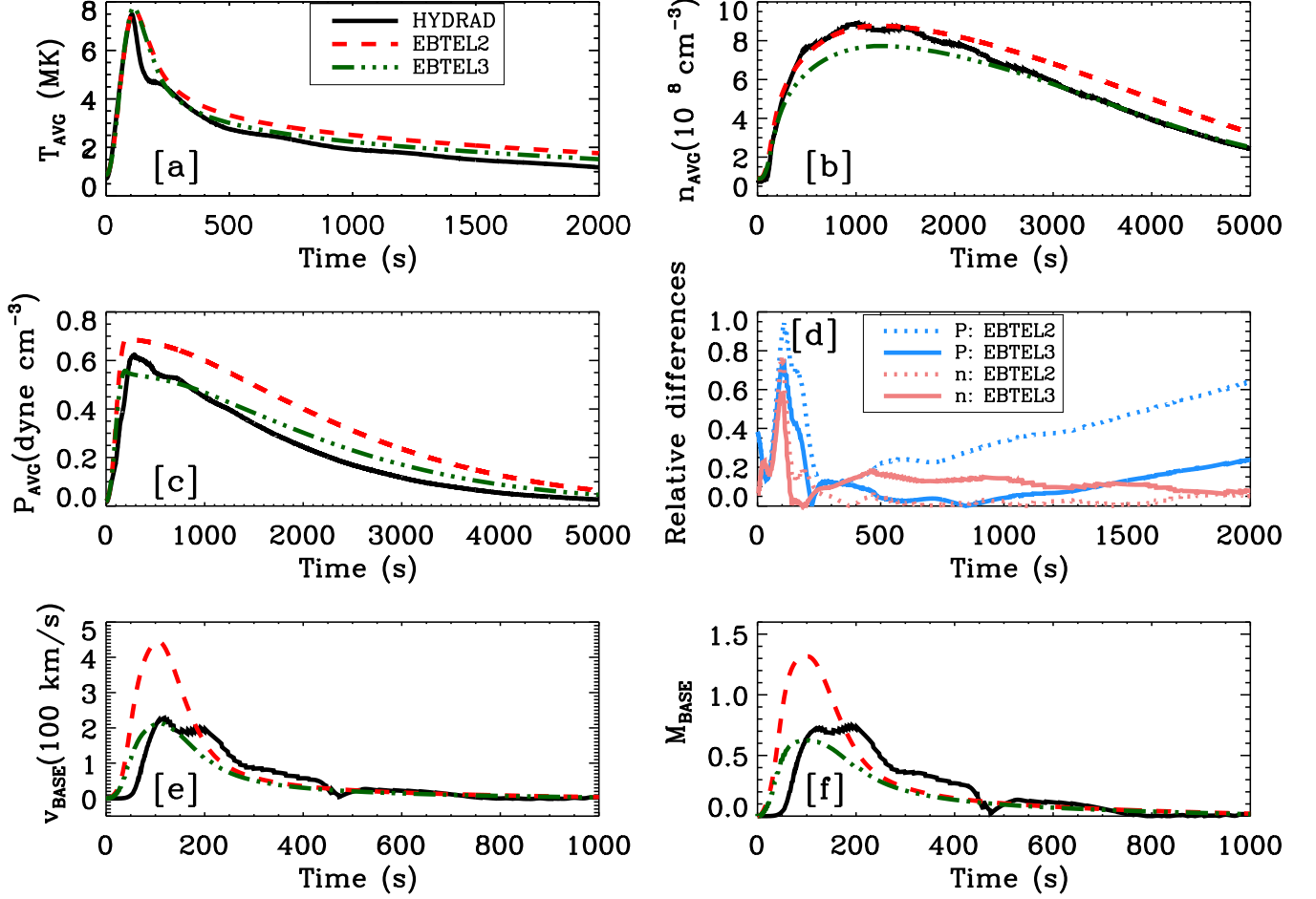


Figure 8. As in Figure 4 but for Case 5: A 50  $Mm$  loop receiving  $5.0 \times 10^9 \text{ ergs cm}^{-2}$  in 200 s.

and that of the heating functions may be used as a diagnostic; when this ratio  $\gtrsim 2$ , flows in HYDRAD approach or exceed supersonic velocities. Since the heating functions have symmetric triangular profiles, their FWHM is simply half of the total duration.  $M_0$  profiles, however, have no concrete shape, hence we resort to finding it numerically by implementing the definition of FWHM. We tabulate these ratios in table 2 for each case along with the maximum Mach number predicted by HYDRAD. A shock should produce a local increase in average temperature in the corona, i.e., a local peak at some time apart from the peak which corresponds to maximum direct heating. The presence of such local peaks in  $\bar{T}$ , and sonic-supersonic flows at the base in HYDRAD is seen in cases where the ratio of FWHMs of  $M_0$  and the heating function is  $\gtrsim 2$ . In such cases there is a large departure from  $M_0$  predicted using EBTEL3 results. Hence if this ratio  $\gtrsim 2$ , the Mach numbers obtained with EBTEL3 should be treated with caution.

#### 4. SUMMARY AND DISCUSSION

Understanding the complete plasma dynamics in coronal loops is important for understanding the energetics of the corona. Under the assumption of an absence of cross-field conduction, these loops can be modeled reasonably well using field aligned hydrodynamical simulations viz., HYDRAD. However, if estimates of the evolution of loops in more realistic scenarios where thousands of elemental strands are present and multiple heating events are involved, field aligned simulations are computationally expensive. Even for cases of a monolithic loop, obtaining quick and approximately accurate estimates of loop evolution over a wide range of parameters, 0D simulations like EBTEL provide a useful alternative.

Cargill et al. (2012b) and Klimchuk et al. (2008) had assumed subsonic flow exists at all stages and hence neglected the kinetic energy term in the energy equation. While this assumption holds good during most of the evolution of

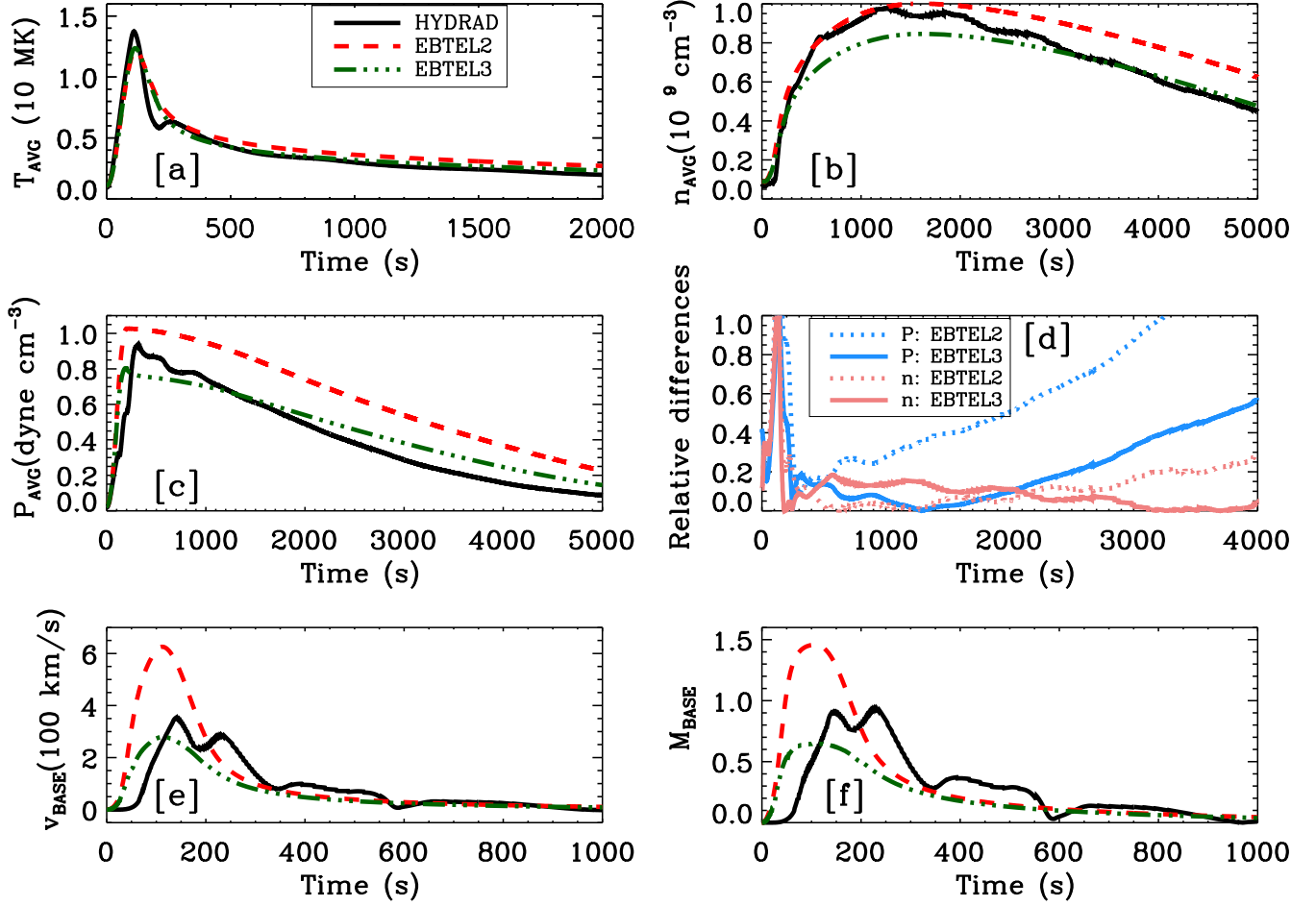


Figure 9. As in Figure 4 but for Case 6: A 75 Mm loop receiving  $1.125 \times 10^{10}$  ergs  $\text{cm}^{-2}$  in 200 s.

Table 2. Ratio of FWHM of profiles of Mach number at base and heating function

Case	Maximum value of $M_0$ in HYDRAD	FWHM of $M_0$ profile in EBTEL3( $r_1$ )	FWHM of input heating profile ( $r_2$ )	$r_1/r_2$
1	0.67	165	100	1.65
2	0.57	396	250	1.58
3	0.49	155	100	1.55
4	0.55	120	100	1.20
5	0.75	193	100	1.93
6	0.94	227	100	2.27
7	1.15	259	100	2.59

loop, it fails during the impulsive phase of some of the heating events. In this paper, we have relaxed the assumption of subsonic flows by not neglecting the kinetic energy term in the energy equation.

In order to solve the equations, we have made the following two assumptions:

$$(i) \left[ \frac{P_0}{P} \right] = \left[ \frac{P_0}{P} \right]_{hse} \left[ \exp \left( \frac{3}{2} M_0^2 \right) \right] \implies \left[ \frac{n_0}{n} \right] = \left[ \frac{n_0}{n} \right]_{hse} \left[ \exp \left( \frac{3}{2} M_0^2 \right) \right]$$

$$(ii) \int_0^L v \frac{\partial P}{\partial s} ds \approx -\frac{1}{2} n_0 \mu v_0^3$$

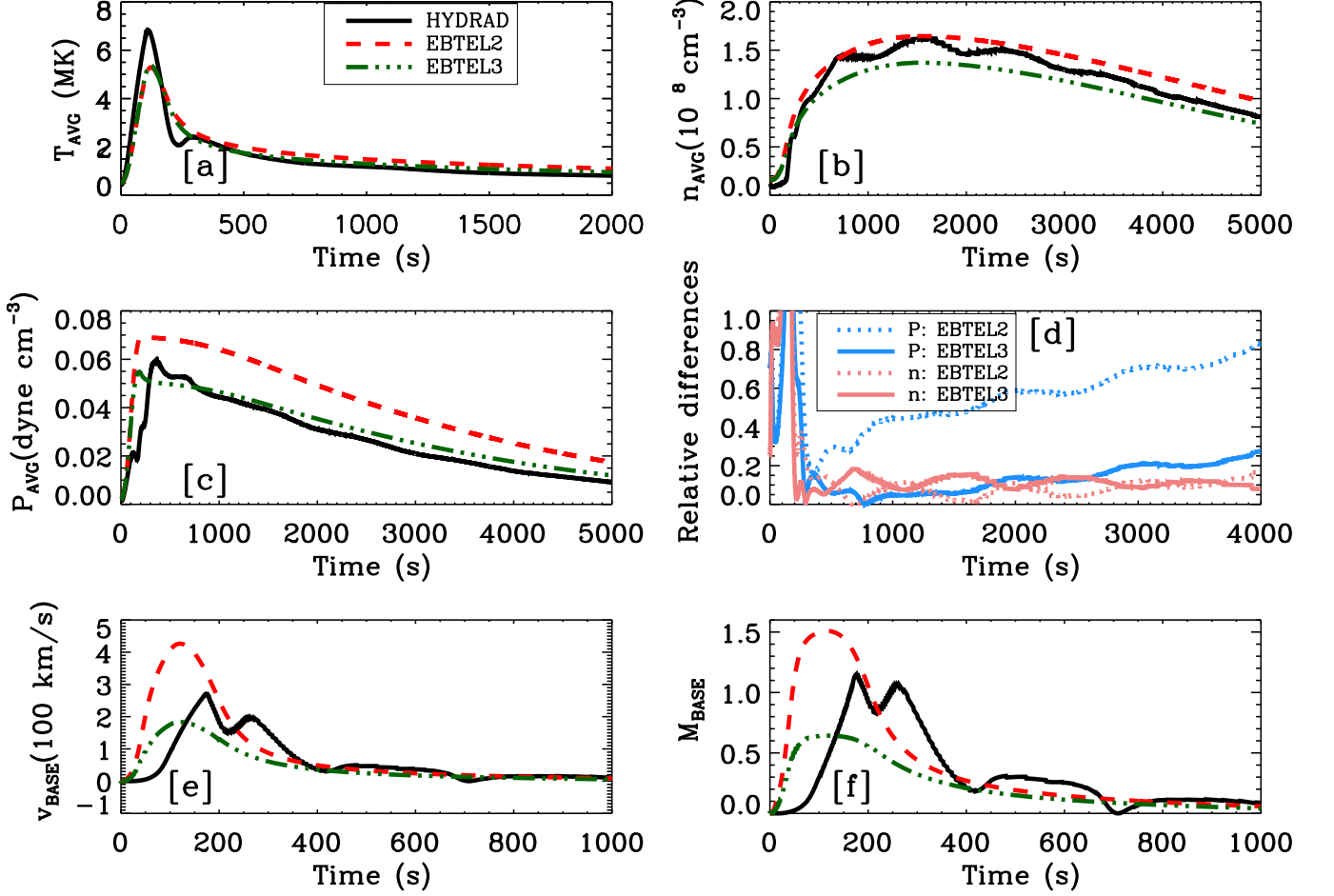


Figure 10. As in Figure 4 but for Case 7: A 60 Mm loop receiving  $6.0 \times 10^8 \text{ ergs cm}^{-2}$  in 200 s.

The results obtained with respect to the plasma dynamics in different kinds of loops by EBTEL3 show significant improvements in average pressure in corona and predicted velocities at coronal base, compared with the results obtained with field aligned simulations using HYDRAD. Though the electron number density produced by EBTEL3 are less accurate than those produced by EBTEL2, the discrepancy still remains less than 20%. The improvement made in pressure estimates by EBTEL3 are larger than the deterioration in electron number density estimates. The main improvement of EBTEL3 over EBTEL2 is however that of velocities, which match better with HYDRAD results. Additionally EBTEL3 guarantees  $M_0$  to remain subsonic if  $M_0$  produced by HYDRAD remain subsonic.

Furthermore, we have developed a simple heuristic to check whether field aligned simulations produce subsonic flows without performing field aligned simulations. This is useful in deciding if the Mach numbers computed by 0D simulations can be trusted, because 0D simulations are not designed to tackle supersonic plasma flows which lead to complicated situations like shocks. For this we look at the ratio of FWHM of profiles of  $M_0$  and heating profiles. If the ratio is larger than 2, Maximum Mach numbers produced at base of corona are close to or even larger than 1. Nevertheless, even in the cases where HYDRAD predicts trans-sonic and supersonic flows, and the Mach numbers derived by EBTEL2 and EBTEL3 cannot be trusted, we find the coronal averages ( $\bar{T}$ ,  $\bar{P}$  and  $\bar{n}$ ) calculated by EBTEL3 to be in good agreement with HYDRAD.

## ACKNOWLEDGMENTS

We thank the referee for many comments and suggestions which significantly increased the lucidity of the manuscript. We thank Dr. Peter Cargill for his valuable comments and suggestions that improved the manuscript. We also thank Dr. Will Barnes for bringing to our attention, a plot showing evolution of various energy terms with time in Barnes et al. (2016). AR acknowledges financial support from University Grants Commission in form of SRF. This work is partly supported by the Max-Planck Partner Group on "Coupling and Dynamics of the Solar Atmosphere" of MPS at IUCAA. VLK acknowledges support from NASA Contract NAS8-03060 to the Chandra X-ray Center, and the hospitality of IUCAA during several visits. The work of JAK was supported by the Internal Scientist Funding Model (competitive work package program) at Goddard Space Flight Center.

*Software:* IDL (<https://www.l3harrisgeospatial.com/Software-Technology/IDL>), and EBTEL (Klimchuk et al. 2008; Cargill et al. 2012b; Barnes et al. 2016)

## APPENDIX

## A. ANALYTICAL SOLUTION TO CUBIC EQUATION

Here, we discuss calculation of velocities in EBTEL2+KE. Using  $P_0 = 2n_0k_B T_0$ , we can re-arrange equation 16 in the following form

$$0 = v_0^3 + \frac{4\gamma k_B T_0}{\mu(\gamma - 1)} v_0 + \frac{2}{\mu n_0} (F_0 + c_1 \bar{n}^2 \Lambda(\bar{T}) L) \quad (\text{A1})$$

The generic cubic equation given by  $v_0^3 + av_0^2 + bv_0 + c = 0$ , for real a, b and c can either have three real roots, only one real root, or repeated real roots (i.e. two roots being same). Two quantities f and q are defined as

$$f = b - \frac{a^2}{3} = \frac{4\gamma k_B T_0}{\mu(\gamma - 1)} \quad \& \quad q = \frac{2a^3}{27} - \frac{ab}{3} + c = \frac{2}{n_0 \mu} (F_0 + c_1 \bar{n}^2 \Lambda(\bar{T}) L) \quad (\text{A2})$$

In above equation we have used the fact that coefficient of  $v_0^2$  is 0 i.e.  $a = 0$ .

A discriminant ( $\Delta$ ) can be defined as

$$\Delta = \frac{q^2}{4} + \frac{f^3}{27} = \frac{c^2}{4} + \frac{b^3}{27} \quad (\text{A3})$$

If  $\Delta$  is positive we have only one real root which is given by

$$v_0 = \left(-\frac{q}{2} + \sqrt{\Delta}\right)^{\frac{1}{3}} + \left(-\frac{q}{2} - \sqrt{\Delta}\right)^{\frac{1}{3}} \quad (\text{A4})$$

For real c,  $c^2$  hence  $q^2$  cannot be negative.  $f^3$  is also positive. Hence we get only one single real root.

However, this method cannot be used directly in EBTEL3. Due to the modifications made to the expression of the base pressure and hence base electron number density in section 2.3 (see equation 28), equation A1 is no longer cubic, and has the form

$$v_0(t)^3 + b v_0(t) + c \exp(d v_0(t)^2) = 0.$$

Therefore, to solve the above equation, we first use an adaptive time grid where the time step  $\delta t$  is set to 0.1 times the smallest of the conductive, radiative, and sonic timescales at time  $t$ . At each time step  $t$ , we use the velocity at the previous time step ( $v_0(t - \delta t)$ ) to find the analytical root of the equation cubic in  $v_0(t)$ , i.e.,

$$v_0(t)^3 + b v_0(t) + c \exp(d v_0(t - \delta t)^2) = 0,$$

The values of the physical quantities obtained in consecutive time steps differ by <10% due to the adaptive time stepping. Note that since the loop evolution always begins from a stationary state, i.e., at  $t = 0$ , velocity is zero.

## REFERENCES

- Barnes, W. T., Cargill, P. J., & Bradshaw, S. J. 2016, ApJ, 829, 31, doi: [10.3847/0004-637X/829/1/31](https://doi.org/10.3847/0004-637X/829/1/31)  
 Bradshaw, S. J., & Cargill, P. J. 2006, A&A, 458, 987, doi: [10.1051/0004-6361:20065691](https://doi.org/10.1051/0004-6361:20065691)

- Bradshaw, S. J., & Mason, H. E. 2003, *A&A*, 401, 699,  
doi: [10.1051/0004-6361:20030089](https://doi.org/10.1051/0004-6361:20030089)
- Cargill, P. J., Bradshaw, S. J., & Klimchuk, J. A. 2012a,  
*ApJ*, 758, 5, doi: [10.1088/0004-637X/758/1/5](https://doi.org/10.1088/0004-637X/758/1/5)
- . 2012b, *ApJ*, 752, 161,  
doi: [10.1088/0004-637X/752/2/161](https://doi.org/10.1088/0004-637X/752/2/161)
- Cargill, P. J., Bradshaw, S. J., Klimchuk, J. A., & Barnes,  
W. T. 2021, Submitted in *MNRAS*
- Cargill, P. J., Mariska, J. T., & Antiochos, S. K. 1995, *ApJ*,  
439, 1034, doi: [10.1086/175240](https://doi.org/10.1086/175240)
- Klimchuk, J. A. 2006, *SoPh*, 234, 41,  
doi: [10.1007/s11207-006-0055-z](https://doi.org/10.1007/s11207-006-0055-z)
- . 2015, *Philosophical Transactions of the Royal Society of  
London Series A*, 373, 20140256,  
doi: [10.1098/rsta.2014.0256](https://doi.org/10.1098/rsta.2014.0256)
- Klimchuk, J. A., Patsourakos, S., & Cargill, P. J. 2008,  
*ApJ*, 682, 1351, doi: [10.1086/589426](https://doi.org/10.1086/589426)
- Priest, E. 2014, *Magnetohydrodynamics of the Sun*,  
doi: [10.1017/CBO9781139020732](https://doi.org/10.1017/CBO9781139020732)
- Rajhans, A., Tripathi, D., & Kashyap, V. L. 2021, arXiv  
e-prints, arXiv:2105.08800.  
<https://arxiv.org/abs/2105.08800>
- Reale, F. 2014, *Living Reviews in Solar Physics*, 11, 4,  
doi: [10.12942/lrsp-2014-4](https://doi.org/10.12942/lrsp-2014-4)
- Subramanian, S., Kashyap, V. L., Tripathi, D., Madjarska,  
M. S., & Doyle, J. G. 2018, *A&A*, 615, A47,  
doi: [10.1051/0004-6361/201629304](https://doi.org/10.1051/0004-6361/201629304)